APPLICATION OF CONTROLLED SPALLING TO THIN-FILM LITHIUM NIOBATE TRANSDUCERS

By

Dennis Rich

Senior Thesis in Electrical Engineering

University of Illinois at Urbana-Champaign

Advisor: Dr. Can Bayram

December 2018

Abstract

The phenomenon of spalling, the peeling of films from substrates based on stress, is investigated for use in production of thin films. Software is developed to understand this process and develop predictions for controlling it. A specific implementation of the controlled spalling method is developed, using electroplating to deposit a stressed film with tunable properties. An original sample holder is developed for efficient performance of this process, and analysis of deposition through scanning electron microscopy and Nomarski microscopy is used to make it repeatable. Stresses are measured through optical profilometry and determined to be too low; conclusions are drawn about future steps necessary to reach the stresses needed for controlled spalling. Steps are also taken to measure the fracture toughness of lithium niobate through nanoindentation. This measurement, not yet made in the literature, makes possible the analysis of controlled spalling of lithium niobate for application to thin-film transducers useful for stress sensing and communications in restrictive form-factor settings such as outer space or the human body.

Subject Keywords: Controlled spalling; Thin film; Sensors

Acknowledgments

Thanks to the University of Illinois (UIUC) Office of Undergraduate Research and the Campus Honors Program for directly sponsoring this work, to the Barry Goldwater Foundation and the UIUC Department of ECE for sponsoring my education, and to the Air Force Office of Scientific Research Young Investigator Program under award number FA9550-16-1-0224, the UIUC Materials Research Laboratory, the UIUC Micro and Nanotechnology Laboratory, and the UIUC Innovative Compound Semiconductor Laboratory.

Contents

1. Introduction 1
1.1 Goal 1
2. Literature Review 2
2.1 Motivation for Lithium Niobate Transducers 2
2.2 History and Dynamics of Controlled Spalling 4
2.3 Application of Spalling to Lithium Niobate 6
3. Description of Research Results 7
3.1 Methods 7
3.1.1 Analysis Software 7
3.1.2 Silicon Thin Film Production 7
3.2 Results 9
3.3 Continued Improvements and Future Work 12
3.3.1 Stress Improvements and Verification 12
3.3.2 Final Production of Samples 13
3.3.3 Extension to Lithium Niobate 13
4. Conclusion 15
References 16
Appendix A: Standalone Spalling Analysis Software Manual 17

1. Introduction

Thin-film devices, two orders of magnitude thinner than conventional electronics, enable unique design opportunities in confined-volume, strenuous settings. These designs take advantage of the low weight and natural flexibility that thin-film brittle materials, which are typically thinner than 50 µm, tend to express. Emerging consumer products that respond robustly to a wide variety of conditions (such as stress) and flexible biomedical implants could be similarly enabled by processes that create thin-films. One such product is the thin-film surface acoustic wave (SAW) transducer.

SAW transducers enable powerful sensing and communications devices with highly tunable environmental and frequency response. SAWs, shallow lattice oscillations produced by the application of electric signals through metal contacts to piezoelectric materials, propagate in a typical device from transmitter to detector, modifying the input electrical signal. SAWs respond measurably to tiny changes in stress (<1 με) [1], allowing accurate sensors, and with adjustment of the contact shape also function as highly tunable bandpass filters for communication. Of all SAW carriers, lithium niobate ($LiNbO_3$) shows the highest coupling efficiency [2] and allows GHz-order transmission for fast data transfer [3] and sensor selectivity [4]. In a thin-film package, its stress-sensing and signal processing capabilities could be integrated seamlessly with environments like outer space and the human body.

1.1 Goal

In this work, I design an application of controlled spalling to fabricate thin films and begin to lay the groundwork to apply it to the first large-scale thin-film $LiNbO_3$ transducers. This method, relying on little sophisticated equipment and no properties of the substrate but its brittleness, allows for substrate reuse, scales economically for production purposes, and is generalizable to all brittle materials. Some future steps are necessary to apply it to $LiNbO_3$, but initial results are demonstrated.

2. Literature Review

2.1 Motivation for Lithium Niobate Transducers

For such a seemingly simple device, the thin film SAW interdigital transducer has received significant attention in academia. The reasons for this are not hard to discern: its powerful applications in communications and sensing and apparently infinite possibility for iterative improvement through different materials and structures make it an ideal target.

A SAW is an acoustic wave that attenuates very quickly as it penetrates its medium; i.e., it is localized on the surface. A SAW transducer converts an electrical signal to a SAW or vice versa through the application of the signal to a piezoelectric material, which reversibly responds to electrical impulse with the generation of internal strain. Thin-film piezoelectric materials are therefore well-suited to this task of carrying surface-localized acoustic signals. In practice, these signals are extremely sensitive to mechanical phenomena, exhibiting coupling with any such events that occur in their presence. Thus, SAW transducers have seen numerous applications as electrical sensors of mechanical events or properties of the material into which they are placed. A transducer can also obtain a very selective frequency response if the electrical contacts are interdigital, since only certain frequencies will be in phase with every other digit as the signal is applied to each one simultaneously. This bandpass property makes SAW transducers extremely useful in mobile communication devices.

However, until somewhat recently, the active frequencies of these sensors and bandpass filters have been limited to below the super high frequency (SHF) range by properties of the piezoelectric materials used. Achieving this range would allow for faster data transfer rates [3] as well as greater sensor selectivity [4]. Properties of the material that we must consider include SAW propagation speed, coupling of the piezoelectric to the interdigital contact, attenuation of the SAW as it propagates, and capacitance internal to the contact/piezoelectric boundary. In Table 1, we define and analyze these properties in common piezoelectric materials.

Table 1

Material	Orientation	v_s (m/sec)	k^2		α_{vac} (dB/usec)	α_{air} (dB/usec)	C_{FF} (nF/m)
			Calculated	Measured			
$LiNbO_3$	Y, Z	3488	0.0504	0.045	0.88	0.19	0.46438
	16.5˚ Y	3503	0.0562	0.048	0.94	0.21	0.46438
	41.5˚ Y, X	4000	0.0578	0.057	0.75	0.3	0.61857
$Bi_{12}GeO_{20}$	001, 110	1681	0.014	0.015	1.45	0.19	0.404522
	111, 110	1708	0.0169	0.017	1.45	0.19	0.404522
	40.04˚	1827	0.0064	—	—	—	0.404522
$LiTaO_3$	ZY	3329	0.0121	0.0093	0.77	0.23	0.443523
	YZ	3230	0.0068	0.0074	0.94	0.2	0.443523
	YX	3148	0.00075	—	—	—	0.47164
	ZX	3205	0.00233	—	—	—	0.443523
	166.65˚	3370	0.0154	—	—	—	0.443523
Quartz	YX	3159	0.0022	0.0023	2.15	0.45	0.050066
	ST, X	3158	0.0014	0.0016	2.62	0.47	0.050339

Taken from [2]. Table of properties of piezoelectric materials at different orientations pertinent to the transmission of high-frequency signals. All properties are described below.

In Table 1, v_s is the propagation velocity of a SAW through a simple thin-film sample. Since higher frequencies travel at higher velocities, maximizing this quantity is essential.

The term k^2 is a measure of the efficiency of the coupling between the piezoelectric and the signal it receives, which is related to the percentage difference between propagation velocity of the material and that of the material with an infinitely thin film on top (the electrical contact). A high k^2 value indicates efficient coupling between these contacts and the free material to which the signal propagates [5].

The terms α_{vac} and α_{air} are the attenuation constants of the material as a signal propagates through vacuum and air, respectively. The final attenuation at a given frequency is given by Eq. 2.1 [2]:

$$\text{Loss (dB/µs)} = \alpha_{vac} \cdot f^2 + \alpha_{air} \cdot f \qquad (2.1)$$

where f is the frequency in GHz. One can see immediately that, although both constants are important even in the low SHF range, the vacuum constant will eventually dominate.

Finally, C_{FF} is the capacitance between a meter of electrical contact and the material. Higher capacitance will, of course, discourage the entry of high-frequency signals [2].

The analysis of these values leads to a clear winner. Lithium niobate ($LiNbO_3$) structures dominate in coupling efficiency, and have above-average propagation velocity and below-average attenuation. The last two properties alone would make it an excellent choice for SHF operation, but the first makes it a practical necessity.

Indeed, thin-film $LiNbO_3$ structures have been demonstrated to be extremely useful as surface acoustic wave (SAW) transducers [6]. Designs have been created that operate easily in the SHF range [3, 4], and that produce coupling coefficients in excess of 0.11 while maintaining stability [7]. In this work, we concern ourselves with the efficient, cheap, and widely applicable fabrication of these $LiNbO_3$ thin-film structures.

$LiNbO_3$ single-crystal thin films can be deposited by chemical vapor deposition on other crystalline materials, most commonly silicon [8]. However, production of thin-films in this manner requires additional deposition and etching. Etching of $LiNbO_3$ is a volatile process that can lead to contamination of other samples, and is best avoided. We propose a better approach: to release a thin film from a bulk substrate after fabrication of that device.

In the past several decades, various methods for brittle thin-film release have been explored. Physical release methods such as epitaxal lift-off [9], which selectively etches a substrate from a thin film, limit the variety of materials that can be used and can damage devices if the etchant is not compatible. Optical methods, meanwhile, include release methods such as laser lift-off [10], which aims a tuned laser at a film-substrate interface which is excited to release upon light absorption. Optical methods are expensive and limited in scalability due to the small-area beam shape. I address the need for a universal mechanical release method, opening the door to $LiNbO_3$ thin-film devices at low cost and accurate thickness.

2.2 History and Dynamics of Controlled Spalling

Controlled spalling has its roots in the mechanical analysis of spalling, stress-induced crack propagation through brittle materials. An understanding of spalling was developed in the late 80s [11, 12]. This extremely general

work explains propagations of cracks through any brittle material, encompassing inorganic semiconductors, ceramics, and more. It understands a crack as an initiation followed by a propagation whose depth is determined only by the forces at the crack tip. These forces are separated into directional modes, each with a well-defined role, as shown in Fig. 1a. Mode I stress, the component of the stress perpendicular to the tensile layer, acts to open the crack. Mode II stress, meanwhile, is the shear stress acting directly at the crack tip, parallel to its propagation.

The magnitudes of both stresses, denoted K_I and K_{II}, are calculated according to Eqns. (2.2) and (2.3) [11].

$$K_I = \frac{P}{\sqrt{2Uh}}\cos\omega + \frac{M}{\sqrt{2Vh^3}}\sin(\omega+\gamma) \qquad (2.2)$$

$$K_{II} = \frac{P}{\sqrt{2Uh}}\sin\omega - \frac{M}{\sqrt{2Vh^3}}\cos(\omega+\gamma) \qquad (2.3)$$

Suo et al. [11] find that, after cracks are initiated, they deflect in a direction that decreases K_{II} as shown in Fig. 1b. When the magnitude of this Mode II stress reaches zero, the crack propagates straight forward in steady state. The result of any crack propagation, therefore, will be a unique, constant depth of cracking (and thin-film thickness) at which mode II stress is eliminated.

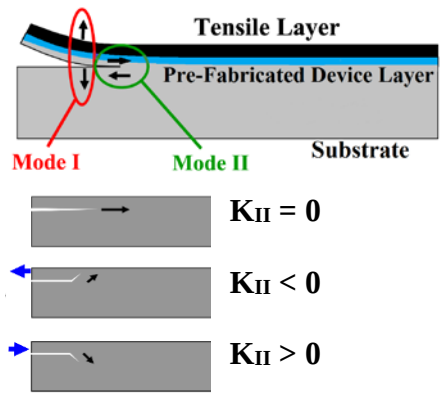

Figure 1. (a) Demonstration of the spalling action, with a substrate-based pre-fabricated device in place [14]. (b) Effects of K_{II} on deflection of the crack tip [14]. Blue arrows are the stresses required to produce that deflection.

However, the application of this theory to the creation of thin-film devices occurred much later. If one deposits a tensile layer of controlled stress and thickness to a bulk material from which a thin film is desired, success can be achieved if the constraints of this theory are followed. The first method of tensile film deposition, and so the first instance of controlled spalling, was implemented by Dross et al. [13]. This work deposited a crystalline tensile layer on Si, ensuring the two layers had mismatched coefficients of thermal expansion, and heated the system to create internal stress formed by the discontinuous lattice expansion at the interface. Such a method was improved upon by Bedell et al. [14, 15], who deposited the tensile layer through electroplating and sputtering, both of which allow for the control of both internal stress and thickness of the tensile layer.

The advantages of these cracks are obvious in hindsight. They propagate through any brittle, uniform material, allowing for processing of any inorganic semiconductor. Furthermore, they propagate indefinitely at a constant depth, allowing for uniform, large-scale thin films. Some disadvantages, however, stem from the reality that not every stressed tensile layer can produce cracking. The magnitude of the Mode I 'opening' stress at the

cracking depth must be larger than the fracture toughness, K_c: an intrinsic property of the material. Higher tensile stress in the layer will serve to increase the opening mode, so processes that produce higher stresses while maintaining predictability are desirable. Furthermore, very thin films (<5 µm) also require very high levels of stress that are difficult to achieve even with electroplating, the most current method.

Still, relying on little sophisticated equipment and no properties of the substrate but its brittleness, the method of spalling method allows for substrate reuse, scales economically for production purposes, and allows for pre-fabrication of devices on the bulk sample before the process is initiated, allowing these to be created in the same way.

2.3 Application of Spalling to Lithium Niobate

Today, controlled spalling is being applied to a wide variety of brittle substrates. In this work, we develop original methods of implementing controlled spalling and begin to extend that list to $LiNbO_3$, whose properties make it ripe for an upgraded method of production, as we have already demonstrated.

As a starting point, we attempt to apply the method of Bedell et al. [14, 15]. We use electroplating to manipulate the stresses in a pre-fabricated $LiNbO_3$ device through thin film deposition, making repeatable observations to obtain excellent control of thickness and stress. With these predictions, we can apply the theory above to calculate the K_{II} stress and predict the resulting behavior of the system, ensuring that it results in a thin film.

3. Description of Research Results

3.1 Methods

3.1.1 Analysis Software

To understand and apply the spalling response of systems to stress, I developed a MATLAB program to calculate these stresses and solve for this steady-state depth based on the physics in [11], described in section 2.2. This program, from material properties of a device substrate, can predict the thickness of the thin-film that could be spalled by depositing a tensile layer of a certain thickness and stress. I added additional features as needed, such as a user interface, graphing capability of varying stress or thickness, and data exporting. This software will be shared online as part of an academic paper, as it has been of considerable predictive use to the lab and would likely help future spalling research greatly. Its manual is given in Appendix A.

3.1.2 Silicon Thin Film Production

The real difficulty of controlled spalling, however, is creating a method of fabrication that agrees with these predictions. With careful theorizing and iterative design, I have implemented a way to control the spalling of silicon, used for cheap testing of the process, by adjusting the stress and thickness of a nickel tensile layer. One related challenge, the adhesion of the tensile layer to the substrate, was met in two ways. First, a thin Ni 'seed' layer was deposited with electron beam evaporation, a high-adhesion method in which a gas of the deposition atom contacts the substrate. Second, adhesion was enhanced with a layer of titanium, which bonds with both the substrate and Ni, deposited between the two materials.

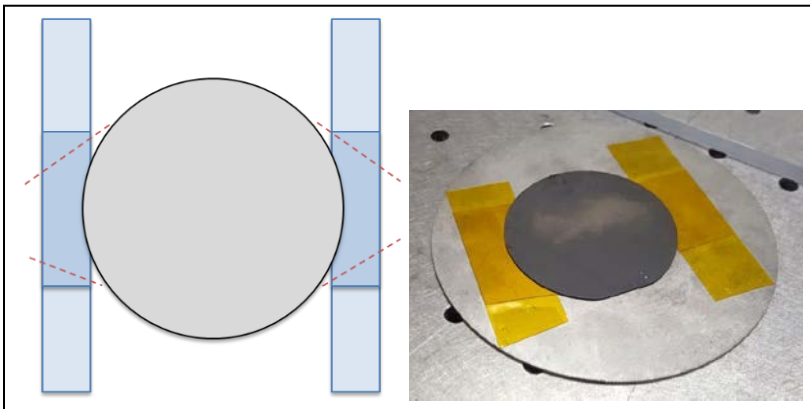

Figure 2. 'Band-aid' method of sample taping.

Initially, there were two problems with this method: first, the deposition system had poor beam control, causing inconsistent layer quality, and second, samples tended to break when removed from the double-sided tape that allowed them to hang upside-down in the deposition chamber. I solved these problems, and rendered deposition consistent, by switching to a new system with better control and developing a method of taping that was easy to remove (shown in Fig. 2). The darker portions, which are not sticky on the bottom, can be cut along the red lines so that

the sample can be lifted from the surface and peeled up. This method is original and applicable to any breakable sample.

The seed layer is unstressed, so I chose electroplating, the transfer of Ni+ ions from solution to a negatively biased substrate, to meet the significant challenge of controlling the thickness and stress of the final tensile layer. The thickness of the deposited Ni layer can be changed by varying the process run time, while its compressive stress is controlled by adjusting the deposition current. I began by carefully designing a 3D-printed, substrate-specific holder to take into account the variable curvature of the sample due to its internal stress. The design of this holder underwent several significant changes before reaching the final iteration shown in Fig. 3.

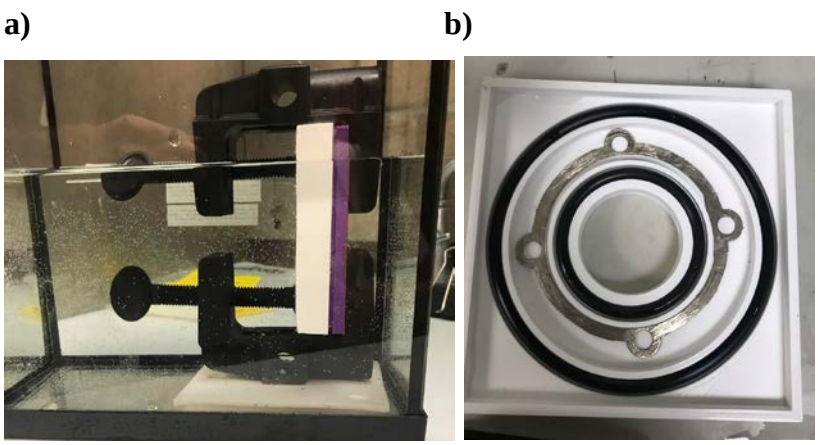

Figure 3. O-ring based sample holder for electroplating (a), with metal contact ring shown in underside of waterproof cavity (b).

The first challenge in designing this holder was mounting of the sample so that electrical contact was established, allowing for negative bias. I implemented a system by which a nickel ring could be screwed into contact with the sample while the latter rested in a fitted depression. The result allowed for easy mounting and minimal handling while maximizing conductive contact with the sample.

However, with this design all was not well. Based on samples like that in Fig. 4a, I hypothesized that Ni was being plated underneath the metal ring (shown in Fig. 3b), which caused cracks to form and propagate outward. Initial fixes, such as putting marker polymer underneath the ring to prevent plating and using copper tape as a conductive surface instead, all failed. Finally, a holder was designed and 3D-printed that uses o-ring seals to prevent nickel deposition on a metal ring that holds the sample down and provides that contact. This holder is the final iteration pictured in Fig. 3.

The holder succeeded in creating successful plating, but it failed to stop the peeling entirely. Peeling occurred only from the edge, which was not plated (shown in Fig. 4b). Therefore, knowing that the failures came from the e-beam step, I attributed the failures to cleanliness: particles get between the e-beam layers and interfere

with adhesion. After implementing piranha cleaning before deposition, this problem disappeared, leaving seed layer deposition consistent. This produced samples like that shown in Fig. 4c.

An obstacle remains, however. Peeling is not the only way a sample can fail. Careful inspection of Fig. 4c will show that the deposited layer is non-uniform, with a lot of imperfections. Nomarski microscopy was used to analyze these samples and confirm the diagnosis. Figure 5a shows the results of this analysis. The many nonuniformities observed led to the testing of a myriad of hypotheses. The final, successful hypothesis was that our failure to completely rinse the samples after electroplating left some of the basic solution on the plated film, which caused corrosion during storage. Better rinsing and drying led to the Nomarski results in 5b. Implementing this rinsing permanently resulted in flawless, consistent samples, shown in Fig. 6.

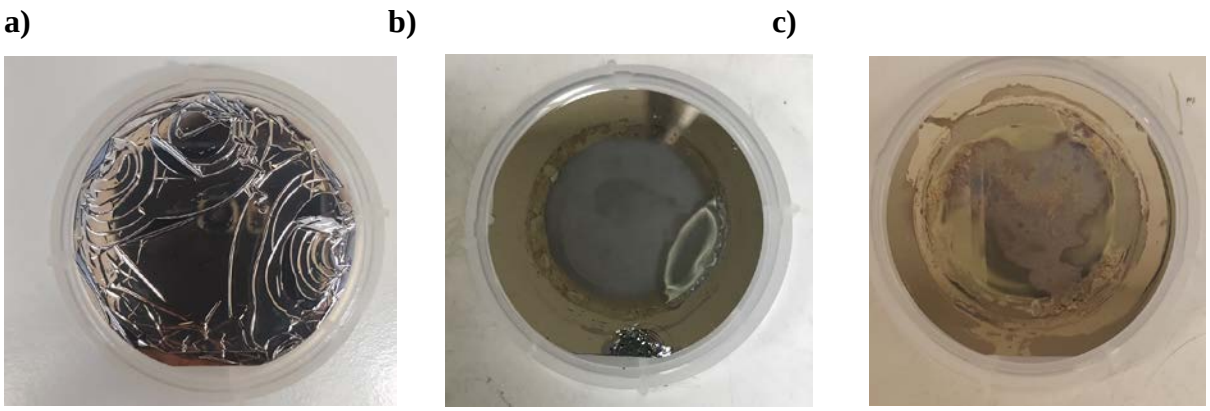

Figure 4. Si samples at different stages of process iteration. (a) The plated layer peels due to cracks propagating inward from the edge. (b) Failures from the edge continue with the o-ring setup. (c) All peeling failures are eliminated.

3.2 Results

Three methods of sample analysis after plating were developed. The first of these is designed to analyze the sample thickness uniformity. The nickel is selectively etched away so that a step height from the top of the electroplated layer to the silicon below can be measured using a profilometer at many

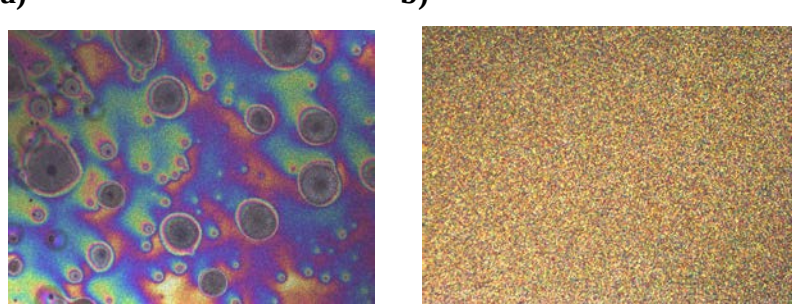

Figure 5. Nomarski surface analysis of un-rinsed (a) and rinsed (b) samples.

different places through the center of the wafer. A wafer so etched is shown in Fig. 6a, and the results of this etching at many different times of plating are shown in Fig. 6b.

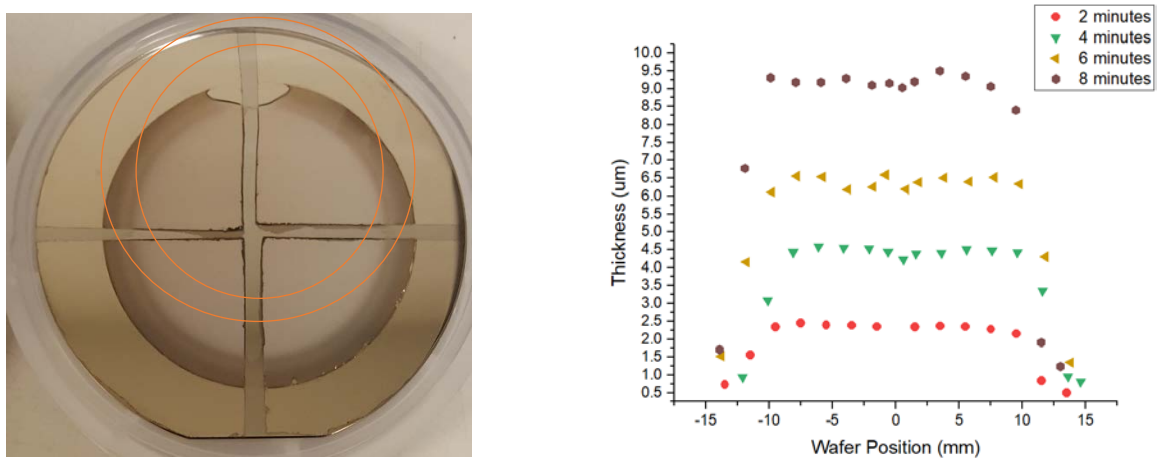

Figure 6. Results of refined etching and thickness uniformity analysis.

Results suggest excellent thickness uniformity except around the edges. This 'drop-off' area is highlighted in red in Fig. 6a, and is almost certainly due to electroplating inhibition by the o-ring. It is yet to be seen if this non-uniformity will affect spalling.

We further analyze the surface by looking at grain size with SEM. Figure 7 shows samples plated for 2, 4, and 8 minutes. Uniformity is good, and longer plating times yield clearly larger grains. This is further support of the validity of the method.

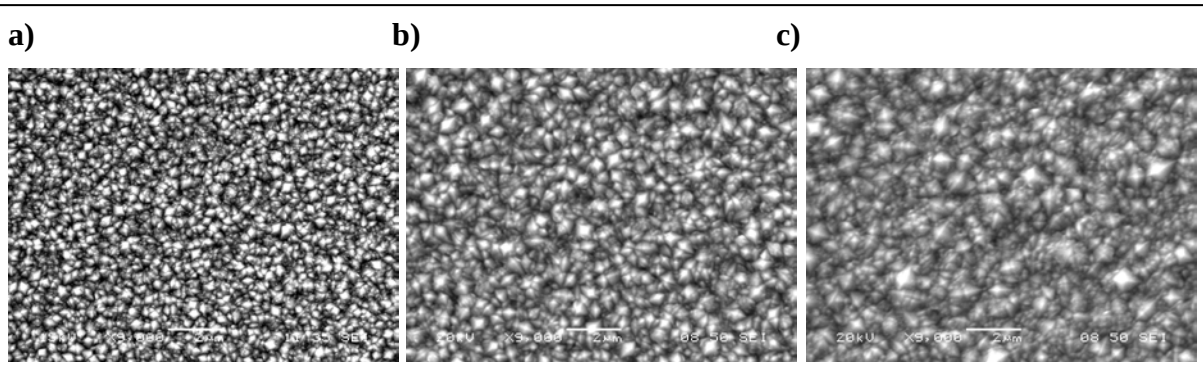

Figure 7. SEM images taken at same scale (bar in each picture is 2 µm). Samples imaged were plated for 2 (a), 4 (b), and 8 (c) minutes.

The final method of analysis optically measures the curvature of the wafer surface, then uses Stoney's equation to calculate stress [16]. The results on different electroplated samples, as well as averaged thickness measurements from etching, are shown in Fig. 8.

Based on these thickness results, the area of the sample, and Faraday's law, one can calculate the efficiency of electroplating assuming a constant nickel density. In Fig. 8, the given thicknesses are averages of the flat parts of the profiles seen in Fig. 6. However, Fig. 6 also shows o-ring interference with the profile, so averaging of every point, including that section, must be performed for the purposes of this calculation. Since the results are linear, they appear to obey Faraday's law as expected. Calculated efficiencies for 2, 4, 6, and 8 minute plated samples are 92.1%, 87.4%, 86.2%, and 88.1%, respectively.

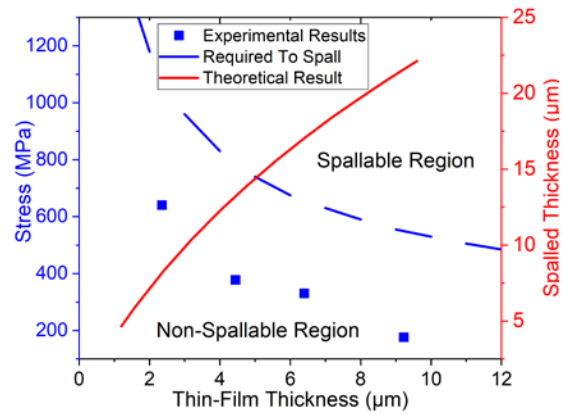

Figure 8. Stresses and thicknesses at different electroplating times, compared to that required to spall according to [11].

Despite failure to enter the spallable region, sporadic spalling has been achieved with the crack initiation setup shown in Fig. 11. These results are shown in Fig. 9.

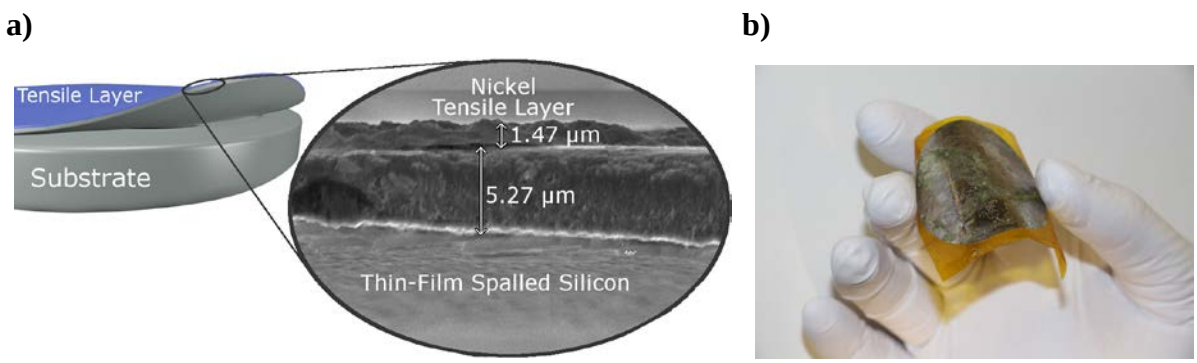

Figure 9. SEM and full-device image of successfully spalled Si wafer.

3.3 Continued Improvements and Future Work

3.3.1 Stress Improvements and Verification

Analysis of the stress results shown in Fig. 8 based on [10] indicates that spalling will not occur at these levels of stress, since they fall below the dotted line. To combat this, the electroplating solution was adjusted to increase stress of the deposited layer. Based on the increase in pH from 3.1 to 3.8 over 171 minutes of electroplating, a forced decrease in pH was investigated and performed. This is further motivated by [17], indicating that increases in pH give worse adhesion, and the expected range is 2.0-4.0. Additionally, chlorides increase deposit stress [18]. It is reasonable to assume that the chloride concentration in the bath has been taken up by previously free-floating H+ ions and decreased stress. The addition of HCl to the solution, it was theorized, should both increase stress and improve adhesion. The reaction would be given by the equations below. HCl disassociates completely, so the proposed chemical formulae can be separated into two: one for the Cl- ions interacting with the nickel chloride, and one for the H+ ions interacting with the boric acid.

$$NiCl_2 \leftrightarrow Ni^{2+} + 2\,Cl^-$$

$$H_3BO_3 + n\,H_2O \leftrightarrow H_{3-n}BO_3{}^{(n)-} + n\,H_3O^+$$

where the latter reaction holds for n = 1, 2, or 3. Therefore, HCl was added to the solution until the pH returned to 3.3. This new bath was tested, but no increase in stress was found.

To ensure the accuracy of the stress measurements plotted in Fig. 8, verification needed to be performed. One method of getting a radius of curvature to do so is optical profiling. In this method, dots are drawn on the sample surface and focused with an optical microscope to get height measurements. In this way, a profile can be measured and fitted as in Fig. 10. The pictured profile yields a radius range of 1.02 to 1.49 m, while the FSM gives a radius of 2.45 m. This trial is not convincing enough for one to assert that the FSM consistently underestimates stress, but the difference is interesting. A more reliable method is needed to convincingly corroborate one of these methods.

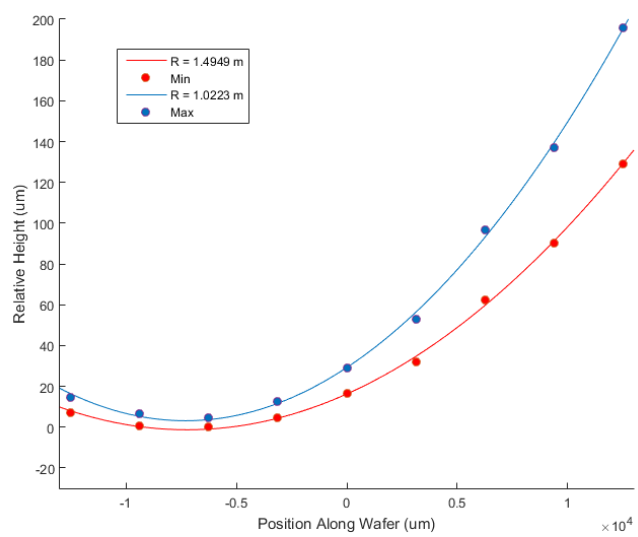

Figure 10. Optical measurement and fit of curvature.

A final challenge that remains in creating a consistent process is measuring the change in solution over time. Keeping record of pH is one method of doing so, but another equally important data point could be the resistivity of samples. Recording changes in resistivity over time could provide valuable insight into the composition of the films, and so the composition of the solution itself [19].

3.3.2 Final Production of Samples

Applying an initial Mode I stress poses another difficulty in which the integrity of the thin-film device must be constantly considered. I have designed and 3D-printed a device by which a sample can be screwed in and a fitted layer of tape applied, shown in Fig. 11.

a) **b)**

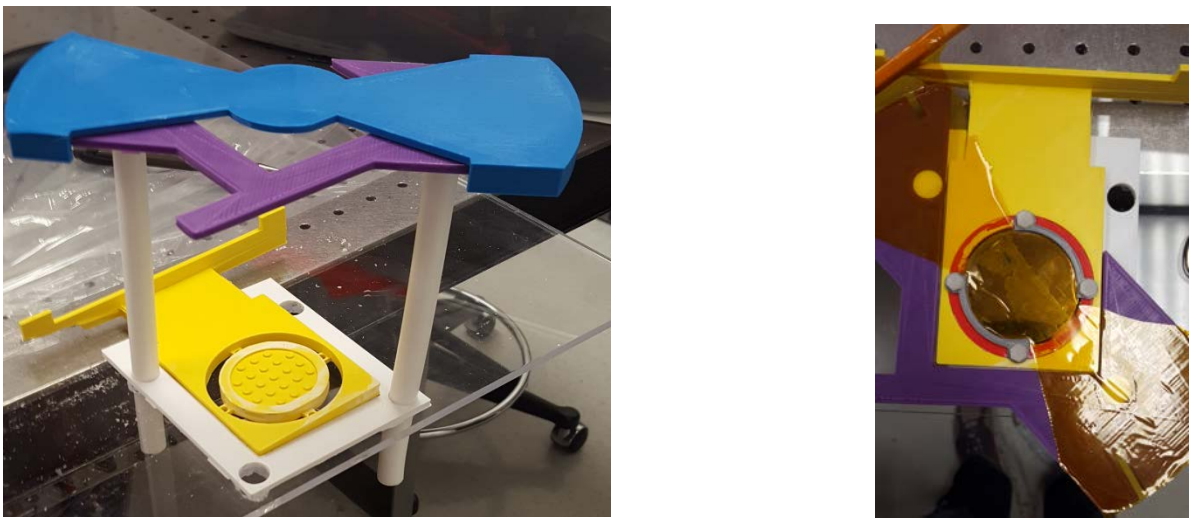

Figure 11. Proposed holder for applying tape to initiate spalling.

Spalling Si substrates is only a step from spalling devices pre-fabricated in Si as in Fig. 1a. I plan to insulate these devices from metal by adding a layer of photoresist between device and tensile layer. Then, controlled spalling will leave a thin-film device insulated from its Ni layer, which I hypothesize can be detached by submerging in photoresist etchant, which is non-harmful to devices.

3.3.3 Extension to Lithium Niobate

Unexpectedly, the fracture toughness of $LiNbO_3$, which quantifies its resistance to spalling, is not available in literature for any crystallographic orientation but Z-cut. I will therefore lay the groundwork for spalling on this material by measuring that of the other orientations. I will use nanoindentation, the creation of small, controlled-force indents in bulk material, to do so, testing my method on Z-cut $LiNbO_3$.

The fracture toughness of any brittle material can be measured and calculated by measuring the crack length produced by nanoindentation. Fig. 12 lays out the two shapes of indentations.

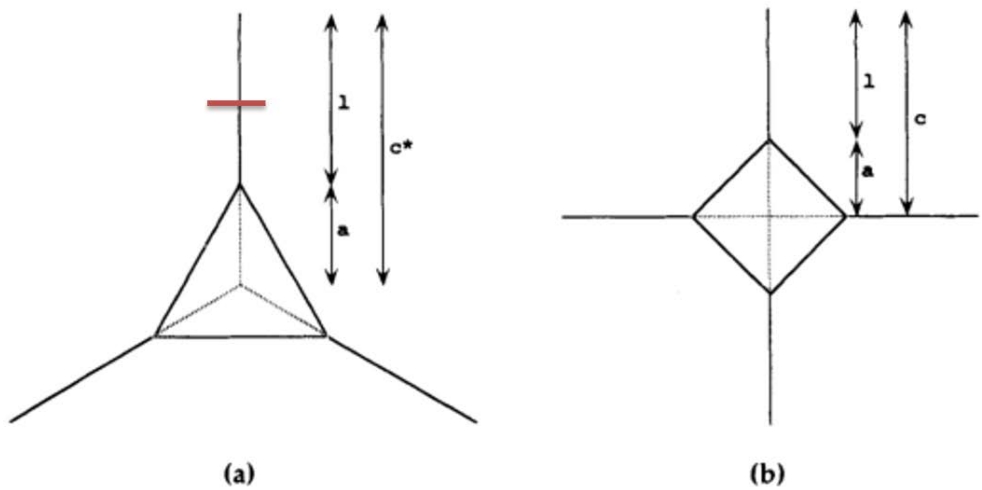

Figure 12 (from [20]). Indentation shapes of the two standard tips. (a) is caused by a Birkovich tip, and (b) is caused by a Vickers tip.

There is some controversy over the merits of Birkovich over Vickers or vice versa. The main difference is likely in the types of cracks they produce. This affects how one uses the *a* and *l* measured in Fig. 12 to calculate a final fracture toughness, shown as K_c in Fig. 13.

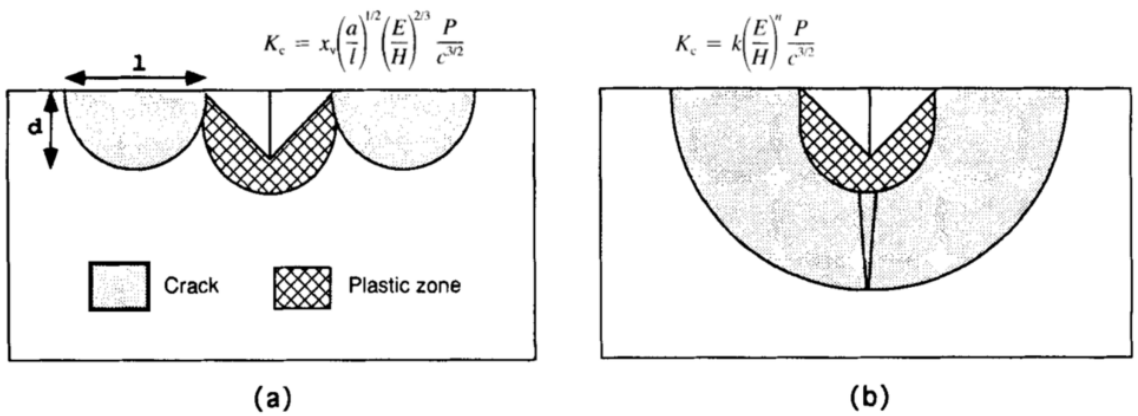

Figure 13 (from [20]). These crack cross sections are viewed as if an incision was made on the red line in Fig. 11. It is hypothesized that (a) is typically caused by a Birkovich tip, and (b) by a Vickers. The methods of calculation in each situation are shown above the respective cross section.

Atomic force microscopy will be used to determine which cracking case occurs from the two cases in Fig. 13, and the respective calculation will be performed.

4. Conclusion

In this work, a method of creating thin films, generalizable to brittle substrates, is created. The steps of seed layer and stressed layer deposition are optimized for repeatability and uniformity using Nomarski microscopy, SEM, and optical analysis. From the results gained by this analysis, a new taping method to reduce sample breakage (Fig. 2), electroplating holder to waterproof the sample (Fig. 3), and setup to initiate spalling with tape (Fig. 11) are developed and built. Analysis of the process shows excellent thickness uniformity (Fig. 6) and grain uniformity (Figs. 5 and 7). However, not enough stress in the sample is observed to spall (Fig. 8) based on the software created for analysis, despite the attempted fixes of optically verifying the stress measurement and changing the composition of the solution. To improve this in the future, I could further change the composition of the solution, seeking out new chemicals that increase deposited stress.

Separately, the deficiency in literature is observed. The fracture toughness of $LiNbO_3$ in certain crystallographic orientations has never been measured. I initiate performance of this measurement, performing nanoindentation on $LiNbO_3$ samples. I will measure the results of this indentation and get values of fracture toughness for their orientations.

References

[1] H. Xu et al., Appl. Phys. Lett. 112, 093502 (2018).

[2] A. Slobodnik, Proceedings of the IEEE 64, 5 (1976).

[3] T.-C. Lee, J.-T. Lee, and M. A. Robert, Appl. Phys. Lett. 82, 191 (2003).

[4] H.-L. Cai et al., Biosens. Bioelectron. 71, 261 (2015).

[5] F. S. Hickernell, Proceedings of the IEEE 64, 5 (1976).

[6] C. C. W. Ruppel, et al., International Symposium on Acoustic Wave Devices for Future Mobile Communication Systems, (2001).

[7] X. Chen and M. A. Mohammad, Journal of Vacuum Science & Technology B, 33, 6 (2015).

[8] Y. Sakashita and H. Segawa, Journal of Applied Physics 77, 11 (1995).

[9] E. Yablonovitch, T. Gmitter, J. Harbison, and R. Bhat, Applied Physics Letters 51, 2222 (1987).

[10] W. S. Wong, A. Wengrow, Y. Cho, A. Salleo, N. Quitoriano, N. Cheung, and T. Sands, Journal of Electronic Materials 28, 1409 (1999).

[11] Z. Suo and J. W. Hutchinson, International Journal of Solids and Structures 25, 1337 (1989).

[12] M. Thouless, A. Evans, M. Ashby, and J. Hutchinson, Acta Metallurgica 35, 1333 (1987).

[13] F. Dross et al., Appl. Phys. A 89, 149-152 (2007).

[14] S. W. Bedell, D. Shahrjerdi, K. Fogel, P. Lauro, B. Hekmatshoar, N. Li, J. Ott, and D. K. Sadana, ECS Transactions 50, 315 (2013).

[15] S. W. Bedell, C. Bayram, K. Fogel, P. Lauro, J. Kiser, J. Ott, Y. Zhu, and D. Sadana, Applied Physics Express 6, 112301 (2013).

[16] X. Feng, Y. Huang, H. Jiang, D. Ngo, and A.J. Rosakis, Journal of Mechanics of Materials and Structures **1**, 1041 (2006).

[17] J. Edwards, *Electroplating: A Guide for Designers and Engineers* Committee for the Promotion of Electroplating, (1983).

[18] P.A. Kohl, *Electrodeposition of Gold*, John Wiley & Sons, New York, NY, 201, (2010).

[19] J.K. Luo, M. Pritschow, A.J. Flewitt, S.M. Spearing, N.A. Fleck, and W.I. Milne, J. Electrochem. Soc. 153, D155 (2006).

[20] R.D. Dukino and M.V. Swain, Journal of the American Ceramic Society 75, 3299 (1992).

Appendix A: Standalone Spalling Analysis Software Manual

SPALLING DEPTH CALCULATOR USER MANUAL

Dennis Rich and Dr. Can Bayram, 2018

Innovative Compound Semiconductor Laboratory, University of Illinois at Urbana-Champaign

Table of Contents

Introduction 1
- Motivation for Controlled Spalling 1
- Basics of Software Calculation 1

How to Use 2
- Getting Started 2
- Advanced Features 2

Theoretical Calculations 3
- Large-Scale Algorithm 3
- Stress Intensity Calculation 4

References 4

Introduction

Does spalling apply to my system, and how is it calculated?

Motivation for Controlled Spalling

Controlled spalling can be induced through applying, to the top of a device fabricated in a substrate, a tensile layer (usually 2-15 μm) whose stress causes a thin film of the part of the substrate containing the device to spall (as in Fig. 1a). Relying on little sophisticated equipment and no properties of the substrate but its brittleness, this method allows for substrate reuse, scales economically for production purposes, and is generalizable to all brittle materials. With this technology, efficient, stress-tolerant, and radiation-resistant inorganic thin-film electronics could be used widely in consumer products, medicine, aviation, and much more [1]. This software predicts the propagation of a crack after this tensile layer is applied. If your system is uniform and the substrate is brittle, its calculations will hold.

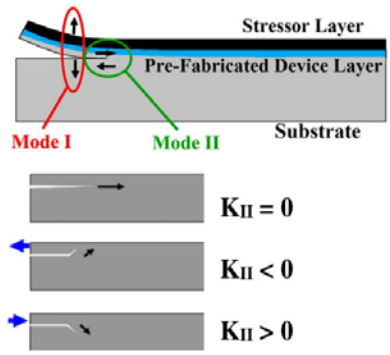

Figure 1 (adapted from [1]). In (a), a demonstration of the spalling action, with a substrate-based pre-fabricated device in place. In (b), the effects of KII on deflection of the crack tip. Blue arrows are the stresses required to produce that deflection.

Basics of Software Calculation

The stress at the crack tip is separable into modes, each with a well-defined role, as shown in Fig. 1a. The stress acting to open the crack, perpendicular to the film-substrate interface, is Mode I stress, whose value (denoted K_I) determines whether spalling will occur. Mode II stress is the shear stress acting parallel to the progression of the crack, serving to deflect the crack upward or downward depending on its sign. K_I and K_{II} are functions only of depth and tensile layer stress, so the steady-state cracking depth is reached when K_{II} is zero [2]. This software calculates K_I and K_{II} as a function of crack depth, determining for a simple set of input parameters where K_{II} reaches zero and the steady-state cracking depth holds. The appendix provides more details about the specifics of the calculation.

How To Use

Basic depth calculations and other useful features

Getting Started

In order to make any calculation, the system's geometry and the properties of its two materials must be known. The properties required are arranged in Table 1.

Stressor Tension	Tensile stress in stressor layer (see Fig. 1)
Stressor Thickness	Thickness of stressor layer (see Fig. 1)
Substrate Thickness	Thickness of substrate (see Fig. 1)
Digits after Point	The depth of spalling will be calculated to this accuracy, to save computation time.
Stressor Material	Input stressor material from drop-down. For details on inputting your own or using the min-max feature, see 'Advanced Features'
Substrate Material	Input substrate material from drop-down. For details on inputting your own or using the min-max feature, see 'Advanced Features'

Table 1. Description of parameters required for spalling depth calculation.

Upon pressing the 'calculate' button, the 'Stresses at Different Depths in Substrate' graph will populate and results will appear in text above it. The graph is of the same form as Figure 4 from [1]. K_I and K_{II}, the stress intensity factors shown in Fig. 1 and discussed in the 'Basics of Software Calculation' section, are calculated for a range of substrate thicknesses and plotted. The point at which $K_{II} = 0$, known to be the steady-state cracking depth from [2], is indicated with a pink line and in text to the right of the 'Calculate' button. The K_I stress at this depth is compared to the K_{ic}, or fracture toughness, entered for the substrate. If it is higher, spalling will occur.

Advanced Features

Stressor and Substrate Material Properties

If a material not in the drop-down list is desired, one may simply enter the Poisson's ratio and Young's modulus for that material (putting the same value in the Min and Max boxes if no uncertainty is required). If a material's values look wrong, select that material from the drop-down menu, then select 'Other' from the same menu and the values will be editable.

It's possible, but not necessary, to visualize the effect on the system if either of these parameters aren't precisely known. Enter the lower bound on that property in the 'Min' box, and the upper bound in the 'Max' box. The resulting 'Stresses at Different Depths in Substrate' graph will display the results at both of those bounds, and calculate final results based on the average of the parameters themselves.

Graph Type

In addition to visualizations of the stress intensity factors, one can vary parameters to explore how they change features of the results. These are intended for design purposes, when one is attempting to calculate the best parameters for their system. The options, which are revealed when the 'Critical Depth vs…' radio button is selected, are explained in Table 2.

Critical Depth vs. Tension	This title is misleading. Critical depth is not affected by adjusting the stressor tension: only the K_I stress at spalling. This is reflected in the axis titles. One can save the data to determine what tension is required to spall a given system.
Critical Depth vs. Substrate Thickness	The substrate thickness, centered on that entered before calculation, is varied and its impact on the critical depth shown. *Spalling is not guaranteed given the tension entered!*
Critical Depth vs. Stressor Thickness	The stressor thickness, centered on that entered before calculation, is varied and its impact on the critical depth shown. *Spalling is not guaranteed given the tension entered!*

Table 2. Description of types of graph beyond the default that can be calculated.

Any of these graphs can be saved as a .csv file or a .fig (MATLAB-specific editable file format).

Theoretical Calculations

Structure of calculation and equations used from [2]

Large-Scale Algorithm

[2] is used to calculate K_I and K_{II} stresses at a given substrate depth (described in the 'Stress Intensity Calculation' section). This calculation is repeated, first to create the 'Stresses at Different Depths in Substrate' graph at reasonable resolution, and then in increasingly small intervals over which the first zero crossing is observed to the precision requested by the user input 'Digits after Point'.

Stress Intensity Calculation

First, the shear modulus, μ, is calculated for both materials from Poisson's ratio, υ, and Young's modulus, E, from the well-known Eq. 1 for isotropic materials.

$$\mu = \frac{E}{2(1+\nu)} \tag{1}$$

From here, our goal is to calculate the parameters from Eq. 11 in [2], reproduced below.

$$K_{\mathrm{I}} = \frac{P}{\sqrt{2Uh}} \cos\omega + \frac{M}{\sqrt{2Vh^3}} \sin(\omega+\gamma)$$

$$K_{\mathrm{II}} = \frac{P}{\sqrt{2Uh}} \sin\omega - \frac{M}{\sqrt{2Vh^3}} \cos(\omega+\gamma)$$

Next, α and β are calculated from Eq. 1 in [2], from which the stiffness ratio **Σ** from Eq. 2 in [2] is calculated. From these and λ, which is a geometrical ratio pictured in Fig. 2 of [2], Δ and Δ_0 can be calculated from Eq. A1 in [2]. At this point, Eqs. A3 and A5 are evaluated to get A, A_0, I, and I_0, which lead us to calculation of C_1, C_2, and C_3 from system A7.

Only at this point can parameters from Eq. 11 actually be calculated. P and M are found in Eq. A6, while γ, U, and V are found from system A8. h is simply the thickness of the tensile layer, leaving only ω to be calculated.

Tables 4 and 5 in [2] discuss the calculation of ω. They suggest that, although higher precision can be achieved by tailoring it to the system, the approximation that ω = 52° is good enough for films that aren't too stiff and crack depths that are large enough. The calculation makes this approximation.

References

[1] S. W. Bedell et. al., ECS Trans. **50**, 315, (2013).

[2] Z. Suo and J.W. Hutchinson, Int. J. Solids Struct. **25**, 1337 (1989).